Electrically Assisted Amplified Spontaneous Emission in Perovskite Light Emitting Diodes

Karim Elkhouly,[1,2,†] Iakov Goldberg,[1,2,†] Xin Zhang,[1,2,3] Nirav Annavarapu,[1,2] Sarah Hamdad,[1,2] Guillaume Croes,[1,2] Cedric Rolin,[1] Jan Genoe,[1,2] Weiming Qiu,[1,#] Robert Gehlhaar,[1,*] and Paul Heremans[1,2,*]

AFFILIATIONS

[1]*IMEC, Kapeldreef 75, Leuven 3001, Belgium*

[2]*ESAT, KU Leuven, Kasteelpark Arenberg, Leuven 3001, Belgium*

[3]*Center for Micro Nano Systems, School of Information Science and Technology (SIST), Fudan University, Handan 220, Shanghai, 200433, China*

[#]Current Address: *Guangzhou Chasing-Light Technology Co.LTD，Huangpu District，Guangzhou，China*

[†]Karim Elkhouly and Iakov Goldberg contributed equally to this work

[*]Authors to whom correspondence should be addressed: robert.gehlhaar@imec.be; paul.heremans@imec.be

Abstract

Metal-halide perovskites have emerged as promising gain materials for thin-film laser diodes. However, achieving electrically excited amplified spontaneous emission (ASE) in perovskite light-emitting diodes (PeLEDs), a pre-condition for perovskite laser diodes, is hindered by the conflicting requirements of high conductivity and high net modal gain of the device stack. Here, we develop a transparent PeLED architecture that combines low optical losses with excellent current injection properties. Using 2.3 ns optical pulses at 77 K, we achieve ASE with a threshold of 9.1 μJ cm^{-2}. Upon sub-μs electrical excitation at 77 K of the same device, we achieve current densities above 3 kA cm^{-2} with irradiance values above 40 W cm^{-2}. Notably, co-pumping the PeLED with optical pulses that are synchronized with the leading edge of an intense electrical pulse results in a reduction of the ASE threshold by 1.2 ± 0.2 μJ cm^{-2}, showing that electrically injected carriers contribute to optical gain. To further assess the feasibility of a perovskite

semiconductor optical amplifier (SOA), we probe the PeLED with 1 μs-long optical excitation and observe continuous-wave (CW) ASE at a threshold of 3.8 kW cm^{-2}. Finally, we show that such intense electrical pulses generate electroluminescence brightness levels close to half the irradiance produced by CW optical pumping at the ASE threshold. This work shows that perovskite SOAs and injection lasers are within reach using this type of transparent PeLEDs.

KEYWORDS: metal halide perovskite, laser diode, amplified spontaneous emission, electrical pulsing, continuous wave

Main Text

Metal-halide perovskites have gained considerable attention owing to their unique optoelectronic properties, rich chemistry, and processability. These semiconductors have exhibited remarkable performance in photovoltaics[1–3], light-emitting applications[4–8], photodetectors[9,10], and beyond. Furthermore, metal-halide perovskites hold promise as gain media for lasers, largely because of their high optical gain values[11,12], low defect densities[13,14], and high photoluminescence quantum yields[15]. Recent major achievements such as the excitation of amplified spontaneous emission (ASE) and lasing from isolated films[16,17] and operational LED-like devices[18,19], the demonstration of room-temperature (RT) and cryogenic continuous-wave (CW) lasing under optical excitation[20,21], and a large library of efficient resonator designs[22–25] make the prospects of perovskite-injection lasing very bright.

The challenge of achieving electrically pumped ASE in perovskite LEDs (PeLEDs) stems from the complexity of the electro-optic co-design for the complete device stack. On the one hand, a PeLED needs to operate at extreme current densities in the kA cm^{-2} range while maintaining a high internal quantum efficiency (IQE)[26]. This imposes strict heat management requirements on the PeLED. The use of small-scale devices, heat spreaders, nanosecond electrical pulses, cryogenic cooling, and more conductive functional layers has proven to be effective in combating Joule heating[27–31]. On the other hand, the device stack must be carefully designed to allow for a high net modal gain[32]. Highly conductive electrical contacts such as Al or Ag are characterized by high extinction coefficients in a wide spectral range that overlaps with the perovskite gain bandwidth (Supplementary Fig. S1). The electrodes cannot be moved sufficiently far away in either vertical or lateral direction without sacrificing the device conductivity[33–35]. Despite the high refractive index of the perovskite gain media ($n \approx 2.0$ - 2.6), the guided modes leak into the contact layers, increasing the ASE threshold[19]. This trade-off between the device conductivity and optical losses lies at the heart of realizing thin-film semiconductor optical amplifiers (SOAs) and, ultimately, perovskite laser diodes.

In this work, we propose a vertical transparent PeLED architecture that considerably lowers free carrier absorption losses while simultaneously delivering excellent electrical injection (Fig. 1a). We utilize 20 nm-thick ITO electrodes (R_{sheet} = 350 – 600 Ω sq^{-1}) on both facets of the device, where the circular active areas are lithographically defined in an Al_2O_3 insulating layer above the ITO anode, following the approach from our previous work[36]. To reduce the parasitic series resistance of the PeLED, we place current-carrying metallic lines (R_{sheet} < 1 Ω sq^{-1}) close to the thin ITO electrodes but sufficiently far away from the recombination zone (Supplementary Fig. S2).

The PeLED stack in this work is based on a double-cation $Cs_{0.1}FA_{0.9}PbI_{2.855}Br_{0.145}$ perovskite with a three-dimensional (3D) morphology sandwiched between a 6,6'-phenyl-C_{61}-butyric acid methyl ester (PCBM; 20 nm)/magnesium-doped zinc oxide (ZnMgO; 20 nm) electron transport bi-layer and a solution-processed [4-(3,6-dimethyl-9H-carbazol-9-yl)butyl]phosphonic acid (Me-4PACz) self-assembled monolayer. The energy band diagram of the PeLED functional layers is displayed in Supplementary Fig. S3. The perovskite growth is modulated by the addition of methylammonium chloride (30 mol. %) to the precursor solution. This produces grain sizes on the order of 100s of nm for the 150 nm perovskite active layer, as revealed by scanning electron microscopy (SEM) analysis (Fig. 1b). This thickness is chosen to facilitate sufficient waveguiding in the device core, whereas thinner perovskite layers are characterized by non-ideal surface coverage. We combine a highly conductive perovskite emitter with thin transport layers to preserve PeLED operation at cryogenic temperatures,[29] which was shown to extend device lifetimes[37], enhance radiative recombination rate[38], and exponentially reduce ASE thresholds[39,40].

First, we study the influence of transparent contacts on the ASE threshold (I_{th}). Consequently, I_{th} values extracted from the double-ITO PeLEDs are benchmarked against those measured from the electrode-free

areas in the sample, which comprise a perovskite gain layer sandwiched between the transport layers. The measurements are acquired under 2.3 ns ($I_{opt,ns}$: 532 nm; 20 Hz) optical excitation, both at RT and at 77 K, where the I_{th} is determined by a characteristic kink in the light input-output curves coupled with a strong spectral narrowing (Extended Fig. 1). We remark that the luminescence is measured only through the sapphire substrate. As a result, the intensity of the ASE is severely underestimated compared to the spontaneous emission since the ASE emission is strongly waveguided in the direction orthogonal to the observation and thus only its scattering is measured[41]. For a contacted miniaturized PeLED with a diameter of 50 μm ($A = 1.96 \times 10^{-5}$ cm^2), RT characterization yields $I_{th} = 379$ μJ cm^{-2} compared to $I_{th} = 198$ μJ cm^{-2} for the electrode-free stack (Fig. 1c). The threshold increase can largely be attributed to free carrier absorption in ITO. Remarkably, by cooling down the sample to 77 K, the contacted PeLED is characterized by a low $I_{th} = 9.1$ μJ cm^{-2}, constituting a 40-fold decrease relative to RT. Compared to the electrode-free stack, transparent electrodes induce a mere 37% threshold increase at 77 K, which can be attributed to the higher modal gain of the perovskite active layer at reduced temperatures. From optical mode simulations, the double-ITO architecture yields optical losses of 246 cm^{-1}, a nearly 4-times reduction compared to conventional PeLEDs (Supplementary Note S1). Finally, by studying the dependence of I_{th} on the PeLED area, we observe that I_{th} gradually increases as the device diameter reduces from 200 μm to 50 μm (Extended Fig. 2). Moreover, no ASE fingerprint appears for the smallest fabricated device with a diameter of 20 μm. Guided light requires a minimum critical optical path length at a given population inversion condition for ASE to be observed[42]. Consequently, devices with larger diameters deliver lower I_{th} due to a greater gain-length product[43,44]

Hereinafter, we explore the optoelectronic operation of a device with an intermediate diameter of 50 μm. Despite the increased optical amplification threshold in reference to larger PeLEDs, a smaller active area is preferred for electrical pumping, as it minimizes the impact of Joule heating and improves current injection uniformity.[27] Due to the low reflectivity of ITO electrodes, the PeLED produces Lambertian

emission and nearly equal light outcoupling from each device facet (Extended Fig. 3). Using sub-µs electrical pulses, we reach high irradiance values above 40 W cm^{-2} (Fig. 1d). Due to the layout limitations, the device rise times are dominated by a resistive-capacitive delay of ~ 200 ns both at 77 K and RT (Supplementary Note S2). However, the PeLED performance at 77 K is distinctly superior compared to another scaled PeLED driven at RT (Supplementary Fig. S6c). or, the PeLED delivers external quantum efficiency (EQE) of around 0.9% at 2900 A cm^{-2} (Fig. 1e) when recorded from the bottom facet. Accounting for the outcoupling, the EQE value translates into an IQE as high as 23.2% at these extreme conditions. The PeLED displays spatially uniform emission even at maximum applied current density (inset in Fig. 1e). There, the normalized EL spectrum displays a pronounced asymmetry and a redshift relative to 200 A cm^{-2} (Fig. 1f). These observations are systematically observed across multiple current densities (Extended Fig. 4). Pinpointing the underlying mechanism is complex; nevertheless, these spectral changes could be attributed to mechanisms such as recombination zone shift[26], quantum confined stark effect[45], or onset of ASE.

In the context of electrically stimulated gain, it is instrumental to approximate ASE threshold carrier density (n_{th}) and consequently threshold current density (J_{th}) by employing optical excitation experiments. By fitting the square root of the transient PL signals – recorded below the ASE threshold at 77 K – to the carrier density (n) rate equation, we estimate $n_{th} \approx 7.3\times10^{17}$ cm^{-3} and $J_{th} \approx 3.0$ kA cm^{-2} for a 50 µm PeLED (Supplementary Note S3). These findings highlight our capability to electrically inject a significant number of carriers, similar in scale to the n_{th} required for attaining ASE through optical pumping. Nevertheless, apart from minor spectral changes towards higher current densities, no clear ASE features emerge under extreme electrical pumping alone.

Having demonstrated PeLED operation at comparable excitation levels under separate optical and electrical pumping, we study the PeLED amplification dynamics under photo-electrical co-excitation. A

fixed 525 ns voltage pulse (V_p), J = 3.5 kA cm^{-2}, is synchronized with a 2.3 ns optical pulse, $I_{opt,ns}$ = 19 µJ cm^{-2}, applied at different time instants relative to the electrical bias. The chosen V_p results in reproducible PeLED operation, whereas higher voltages could cause excessive heat generation, compromising device performance and lifetime. An imaging spectrometer integrates the luminescence signal over a 10 ns gating window, triggered 2 ns before the onset of the optical pulse. A schematic of the experimental setup is provided in Supplementary Fig. S8. As depicted in Fig. 2a, the optical excitation is triggered at four different timestamps: 1) before V_p; 2) within the first 200 ns of V_p (start); 3) at the end of V_p (end); and 4) after V_p. Although the transient luminescence curves in Fig. 2a do not show a significant dependence on the timing of the optical pulse, the integrated spectra vary significantly (Fig. 2b). When the PeLED is optically excited by $I_{opt,ns}$ before V_p, we observe a strong ASE signal towering above the spontaneous emission signal (we refer to this spectrum as "reference PL_{ns}"). A significant current-injection contribution is evident when the two excitation sources are overlaid shortly following the complete build-up of V_p (timestamp "2"). Delaying the optical excitation to the end of V_p (timestamp "3") produces a spectrum that exhibits a marked quenching of the peak signal intensity. In the final pulse train, $I_{opt,ns}$ is applied ~ 250 ns after the termination of V_p (timestamp "4"), producing a similar spectrum to the reference PL_{ns}. Each spectrum can be broken down into two (in the case of standalone optical pumping) or three (with an overlaid electrical pulse) Gaussian distributions. These are denoted as SE (PL), ASE, and SE (EL), representing spontaneous emission from PL, ASE, and spontaneous emission from EL, respectively. The EL contribution remains constant, much like the electrical pulse itself.

By subtracting the reference PL_{ns} spectrum from the three spectra triggered after the onset of electrical bias, we can study the spectral effects occurring due to photo-electrical co-excitation of the PeLED (Fig. 2c). A reference EL signal, acquired in the absence of optical excitation at 3.5 kA cm^{-2}, is overlayed over the modified spectra for comparison. Notably, when the PeLED is co-pumped at timestamp "2", we

observe that the modified spectrum exhibits a narrow feature emerging in the ASE bandwidth. We interpret this pronounced feature as an electrically assisted ASE enhancement. In this biasing scheme, electrically injected carriers contribute to the ASE output beam and significantly modulate its intensity. The pronounced electrically assisted ASE enhancement regresses towards an ASE quenching when the optical pulse arrives near the end of V_p (timestamp "3"). At this current density, the PeLED is continuously accumulating Joule heat, aggravated by intrinsically poor perovskite thermal conductivity[26]. The heat accumulation is evident from the corresponding high-energy tail broadening and clear dip at the ASE wavelength. Since the accumulated heat requires some time to completely dissipate, the ASE intensity remains partially quenched some 250 ns after V_p termination (timestamp "4"). The emission fully recovers to the reference PL_{ns} by the next pulsing cycle (timestamp "1"), as we maintain a low V_p pulsing frequency of 10 Hz to ensure stable and reproducible PeLED performance.

Under preserved EL biasing conditions (J = 3.5 kA cm^{-2}), we excite the PeLED at timestamp "2" with gradually increasing $I_{opt,ns}$ fluences up to 15.6 μJ cm^{-2}. Then, we subtract the optically-excited-only spectra from the corresponding photo-electrically co-pumped spectra produced at the same $I_{opt,ns}$ (Fig. 2d). Prominent ASE features are not apparent from the PeLED for $I_{opt,ns}$ below 7.7 μJ cm^{-2} (Extended Fig. 5), where a symmetric modified spectrum akin to EL spectrum is observed. In contrast, at $I_{opt,ns} \geq$ 7.7 μJ cm^{-2}, we detect a systematically increasing ASE peak under photo-electric co-excitation, where ASE contribution to the total signal becomes more pronounced for higher input fluences. To quantify the effects of electrical pumping, we extract SE (PL) and ASE Gaussian amplitudes (Fig. 2e) by fitting the spectra acquired with and without V_p under variable $I_{opt,ns}$ (Extended Fig. 6a-d). On the one hand, the matching SE (PL) amplitudes grow linearly with input fluence, demonstrating negligible effect from electrical bias on radiative recombination processes. In stark contrast, the ASE Gaussian amplitudes, produced using co-excitation, display a significant shift toward lower $I_{opt,ns}$. There, injected carriers assist in reducing I_{th} by 1.2 ± 0.2 μJ cm^{-2} or by ~ 13% (Extended Fig. 6e-f).

To facilitate a better comparison with electrical excitation, CW optical pumping should be used, as it is characterized by a lower peak excitation intensity and increased Joule heating effects. So far, optically-pumped CW ASE/lasing were achieved predominantly in isolated perovskite films, both at RT and cryogenic conditions[20,21,40]. Herein, we attempt CW optical pumping of the scaled PeLED using a 447 nm laser diode. Fig. 3a shows the evolution of the emitted CW spectra (PL_{cw}) in response to a 500 ns, 15 kW cm^{-2} optical pulse ($I_{opt,cw}$). It is important to note that the excitation laser diode rise time is restricted by the available laser diode driver setup (~ 300 ns at 15 kW cm^{-2}), leading to a slow build-up of the emitted signal. In the absence of electrical excitation, transient PL_{cw} spectra are broken down into SE (PL) and ASE Gaussian functions. Starting near zero, the ASE Gaussian amplitude eventually surpasses that of the SE (PL) Gaussian envelope after ~ 300 ns (Fig. 3b). This is accompanied by the narrowing of the PL_{cw} measured at different delay times, where the spectrum evolves from having a symmetric shape with full width at half maximum (FWHM) ≈ 19.5 nm to showing distinct ASE narrowing (FWHM ≈ 14.5 nm). To quantify the CW ASE threshold, we sweep $I_{opt,cw}$ from 0.3 kW cm^{-2} to 15 kW cm^{-2} using a prolonged excitation duration of 1 µs and monitor the steady-state PL_{cw} spectra (Fig. 3c). By assessing the corresponding spectral linewidths at different $I_{opt,cw}$, we establish a reasonable optically-excited CW ASE threshold of 3.8 kW cm^{-2} (Supplementary Table S1). By fitting the PL_{cw} spectra as a sum of several Gaussian functions (Extended Fig. 7), we observe a distinct kink in the input-output curve for ASE Gaussian amplitude denoting the onset of ASE, while the SE (PL) Gaussian does not show similar behavior (Extended Fig. 7c). The magnitude of both Gaussian amplitudes becomes comparable at maximum $I_{opt,cw}$ due to the fast growth of ASE.

Encouraged by this result, we co-excite the PeLED by synchronizing a 1 µs-long optical pulse with a 300 ns V_p (J = 3.5 kA cm^{-2}), where V_p is triggered 100 ns after the start of the optical pulse and the spectrum is integrated over the entire EL excitation duration of 300 ns (Fig. 3d). Although we observe the appearance of ASE at high $I_{opt,cw}$ (Fig. 3e), its intensity is significantly quenched compared to the one

measured under standalone optical excitation at the same power density (Fig. 3f). Moreover, while both sets of spectra show systematic narrowing at higher optical powers in line with the emergence of an ASE peak, the FWHM of the co-pumped spectra remains larger than those measured under optical-only excitation. Furthermore, in Fig. 3d, a drop in PL_{cw} becomes visible near the end of V_p, but the signal quickly recovers within a few 100s of ns after V_p termination. A more drastic dip in PL_{cw} is observed by co-pumping the PeLED at maximum $I_{opt,cw}$ = 15 kW cm^{-2} and systematically increasing current injection levels (Extended Fig. 8). These observations are consistent with the severe, yet reversible, effects of Joule heating on PeLEDs at intense electrical excitation.

The obtained CW optically-excited threshold of 3.8 kW cm^{-2} provides a more direct measure of the equivalent J_{th} as the optical and electrical pulse widths are similar. As a result, we calculate a J_{th} of ~ 4.6 kA cm^{-2} (Supplementary Note S4). Furthermore, by comparing the PeLED irradiance level emitted at the $I_{opt,cw}$ = 3.8 kW cm^{-2} to the EL emitted from the same PeLED at 3.5 kA cm^{-2} (Fig. 4), we observe that EL reaches irradiance levels close to half that of PL_{cw} levels at the ASE threshold. Based on these observations, one might estimate that the PeLED achieves around 50% of n_{th}. This contrasts with the ASE threshold reduction of 13% under 2.3 ns optical excitation, obtained previously using similar electrical pulsing conditions, suggesting that electrically pumped ASE necessitates higher excitation densities compared to optical pumping, largely due to more pronounced Joule heating.

In summary, we have demonstrated miniaturized transparent PeLEDs which combine reduced optically-pumped ASE thresholds and high IQEs at several kA cm^{-2} at 77 K. Thanks to the double ITO electrodes, we achieve ASE thresholds as low as 9.1 µJ cm^{-2} for a functional PeLED of 50 µm in diameter under 2.3 ns optical pumping. Toward the goal of current-driven perovskite SOAs and laser diodes, we achieve some crucial milestones: 1) Electrically-enhanced optically pumped ASE in a perovskite diode under synchronized 2.3 ns optical and sub-µs (3.5 kA cm^{-2}) electrical co-excitation, whereby electrical driving

reduces ASE threshold by an equivalent energy fluence of 1.2 ± 0.2 μJ cm^{-2} or by 13%; 2) CW ASE in a fully contacted perovskite diode under 1 μs-long optical excitation at a threshold of 3.8 kW cm^{-2}; and 3) PeLED electrical injection that produces ~ 50% of the irradiance level at optically pumped CW ASE threshold. These milestones were achieved with diodes that comprise perovskite gain layers with a 3D morphology.

We believe that an optimized transparent PeLED with faster modulation could achieve CW electrically-pumped ASE at 77 K. Specifically, the electrical rise time should be reduced below the time constant of Joule heating, which we show quenches ASE intensity after about 100 ns. A perovskite laser diode, equipped with a high-quality-factor optical cavity, may support lasing at lower thresholds relative to ASE[46]. However, a challenge persists in properly integrating this cavity while avoiding electrical performance degradation. Finally, perovskite current-driven laser would benefit from a low operating voltage, reduced EQE roll-off at high current densities, along with material innovations such as low-dimensionality high-gain perovskite compositions that do not compromise the device conductivity.

Acknowledgements

The project leading to these results has received funding from the European Research Council (ERC) under the European Union's Horizon 2020 research and innovation programme (grant agreement No 835133).

Author Contributions Statement

K.E. and I.G. contributed equally to this work. K.E. conceived the PeLED stack for high current density operation, designed the experiments, and conducted the photo-electrical characterizations. I.G. conceived, designed, and fabricated the double ITO structure, performed optical modeling, and optimized the stack design for low optical thresholds. X.Z. conceived and fabricated the device stack and functional layers. N.A. and S.H. aided in the optical design of the stack and in performing optical characterizations and modal loss modeling. G.C. acquired the SEM image. W.Q. aided in conceiving the PeLED stack, supervision, and the design of experiments. C.R., R.G., J.G., and P.H. supervised this work. K.E. and I.G. wrote the first draft of the manuscript. All authors revised and approved the final version of the manuscript.

Competing Interests Statement

The authors declare no conflict of interest.

Figures

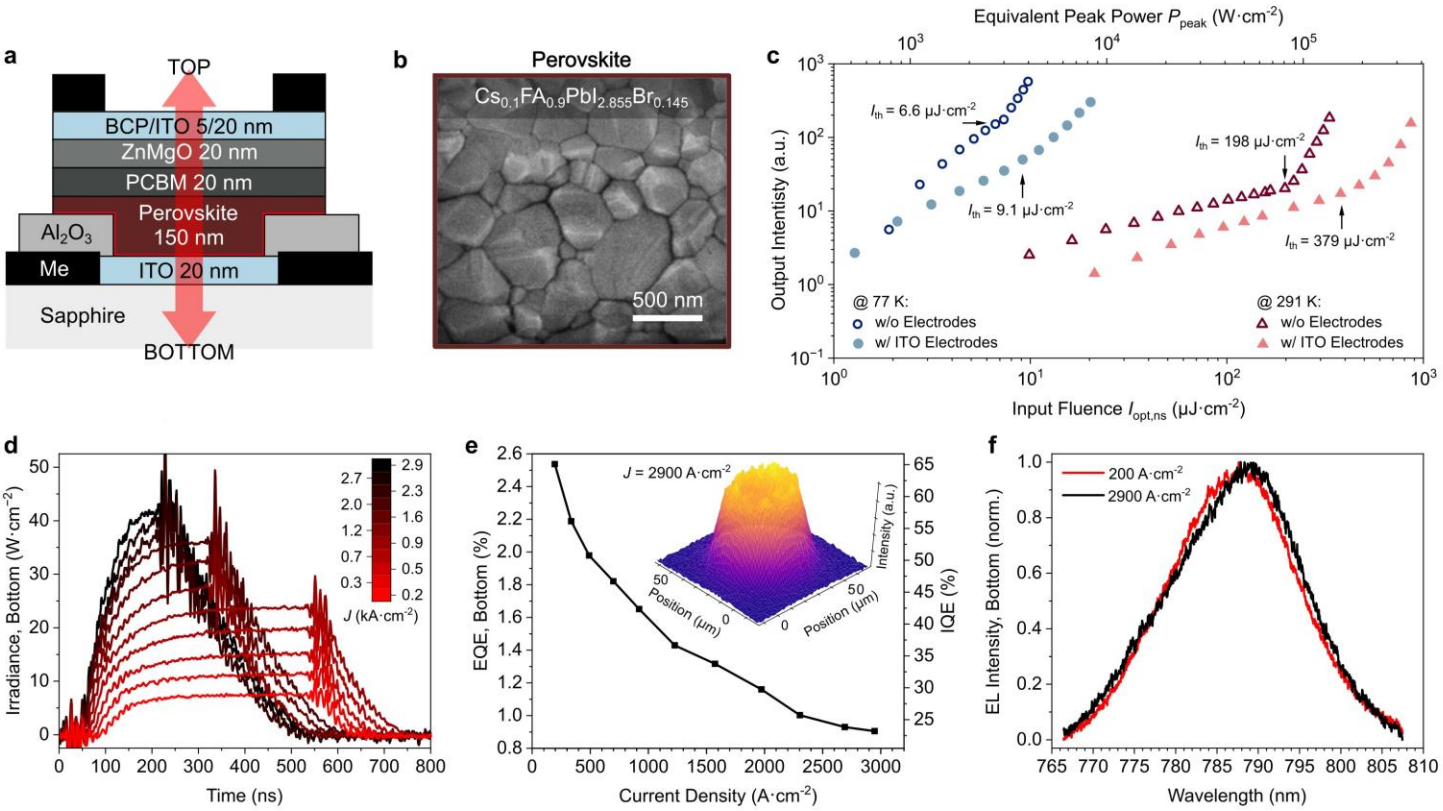

Fig. 1 | Structural and optoelectronic properties of transparent PeLEDs. a, Schematic cross-section. Dimensions are not to scale. **b**, Top-view SEM analysis of the perovskite emitting layer. **c**, Light output intensity as a function of input laser fluence ($I_{opt,ns}$) or an equivalent peak laser power (P_{peak}). **d**, Transient EL response of a PeLED (50 μm in diameter) at 77 K. **e**, EQE/IQE-*J* curve from the PeLED at 77 K. Inset: EL intensity profile from the bottom facet recorded at 2900 A cm^{-2} under 200 ns pulse. **f**, Normalized EL spectra for two current densities from the PeLED recorded through the substrate at 77 K.

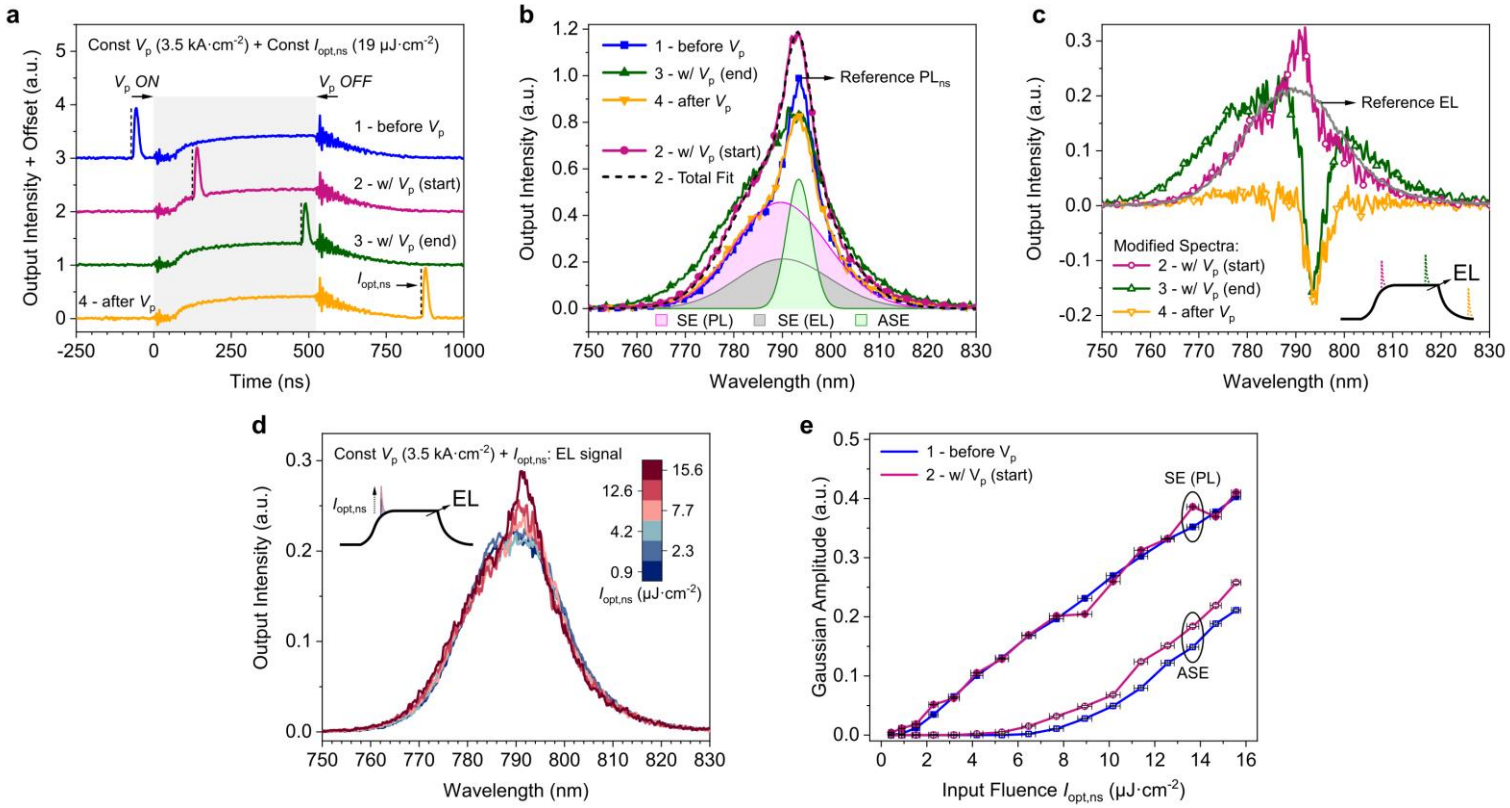

Fig. 2 | Co-pumping dynamics under sub-µs electrical and 2.3 ns optical biases. a, Transient luminescence response produced by a fixed 525 ns voltage pulse (V_p), 3.5 kA cm^{-2}, and a fixed optical $I_{opt,ns}$ = 19 µJ cm^{-2} pulse applied at four different time instants. **b**, Corresponding spectra under photo-electric co-excitation. The fit is performed for a joint spectrum acquired at the rising edge of the electrical pulse. SE (PL), ASE, and SE (EL) represent spontaneous emission from PL, ASE, and spontaneous emission from EL, respectively. **c**, Spectra produced by subtracting the reference PL_{ns} signal. Reference EL spectrum recorded at 3.5 kA cm^{-2} is shown for comparison. **d**, EL contribution to the photo-electric co-excitation signal at variable $I_{opt,ns}$, where $I_{opt,ns}$ is applied following the complete build-up of V_p (timestamp "2"). Standalone PL spectra, produced at the same $I_{opt,ns}$ in the absence of electrical excitation (timestamp "1"), are subtracted from the joint photo-electric spectra. **e**, SE (PL) and ASE Gaussian amplitudes with and without electrical bias as a function of input laser fluence $I_{opt,ns}$. The horizontal error bars represent experimental input energy uncertainty, whereas vertical error bars cover a 68% tolerance interval.

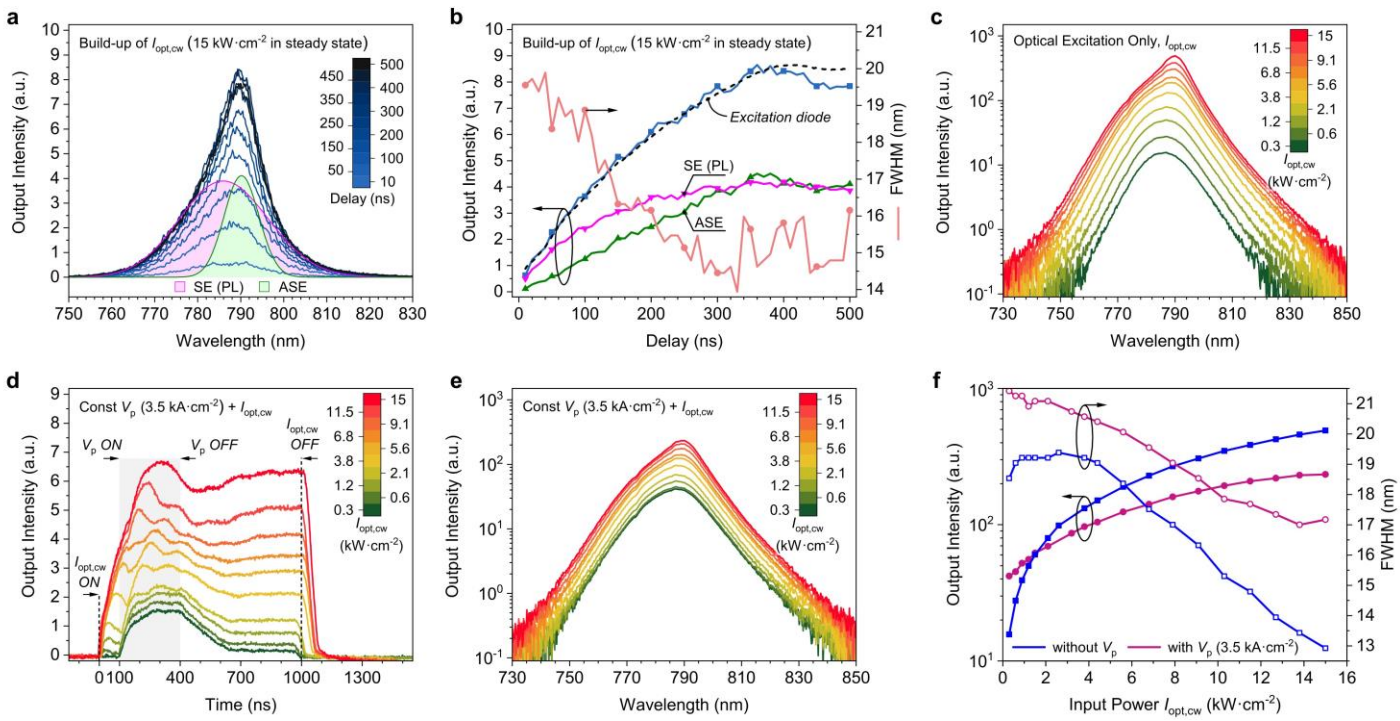

Fig. 3 | Standalone CW optical and CW photo-electrical co-excitation. a, Temporal evolution of PL_{cw} during the build-up of a 15 kW cm^{-2} optical pulse. The spectra are measured within a 10 ns time window. The spectrum at 500 ns is deconvoluted into SE (PL) and ASE Gaussian envelopes, representing spontaneous emission from PL and ASE. **b**, Total light output together with SE (PL) and ASE Gaussian amplitudes (left); and FWHM (right) as a function of delay time. The dashed curve depicts the total output intensity (scaled accordingly) of the 447 nm CW excitation diode. **c**, PL_{cw} spectra under standalone 1 µs CW optical biases. **d**, Transient luminescence response at a fixed 300 ns voltage pulse (V_p), 3.5 kA cm^{-2}, and variable optical $I_{opt,cw}$ pulses. **e**, Joint spectra under simultaneous sub-µs electrical and 1 µs CW optical biases. Spectra in (**c**) and (**e**) are measured throughout the entire 300 ns electrical pulse. **f**, Total light output intensity (left) and FWHM (right) as a function of input laser power $I_{opt,cw}$ with and without electrical bias. FWHM is provided for the total PL_{cw} spectra.

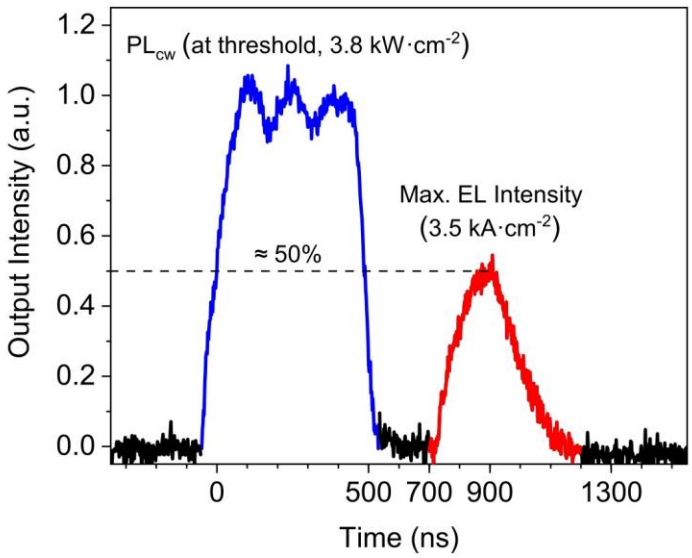

Fig. 4 | Irradiance level comparison under 200 ns electrical and 500 ns CW optical biases in the transparent PeLED. PL_{cw} intensity (blue) is provided at the CW ASE threshold of 3.8 kW cm^{-2}. The maximum achieved EL intensity at 3.5 kA cm^{-2} (red) reaches approximately half that of PL_{cw}.

Extended Figures

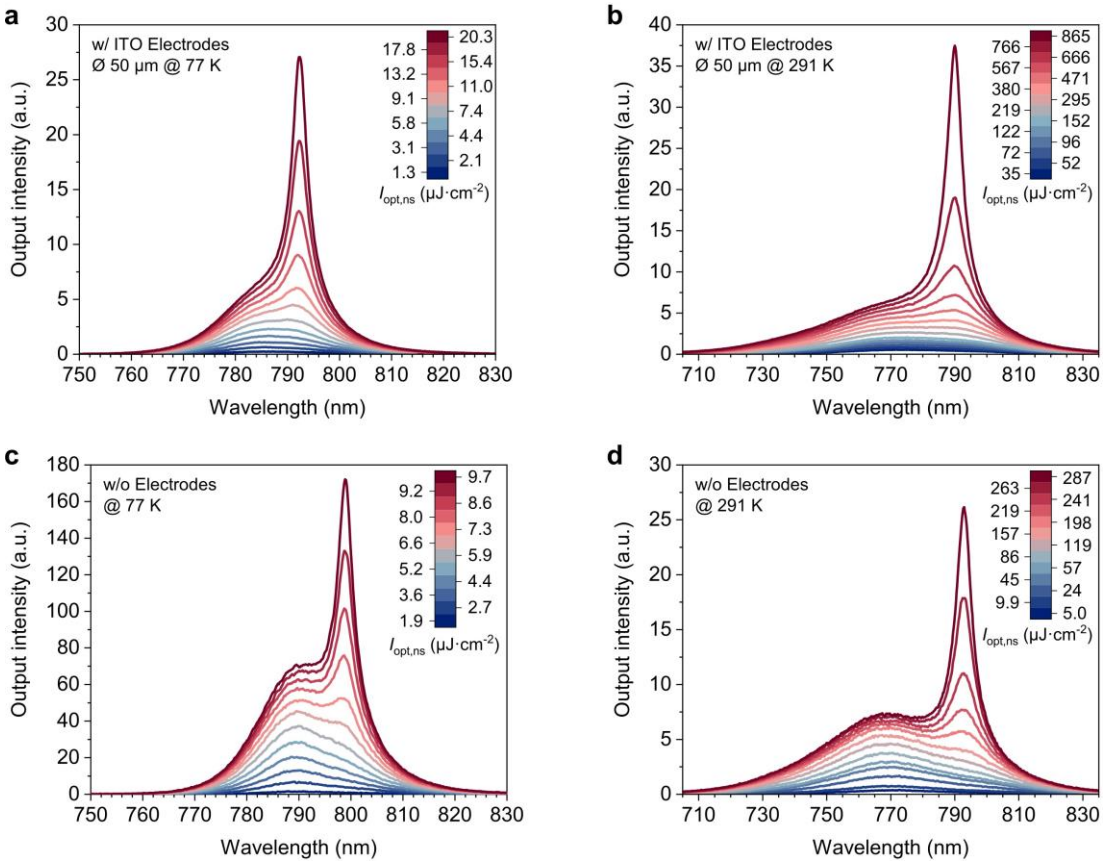

Extended Data Fig. 1 | Optical characterization of PeLED stacks with 2.3 ns $I_{opt,ns}$ pump source. PL output from a PeLED stack with a diameter (⌀) of 50 µm at (**a**) 77 K and (**b**) 291 K. PL output from a contact-free PeLED stack at (**c**) 77 K and (**d**) 291 K.

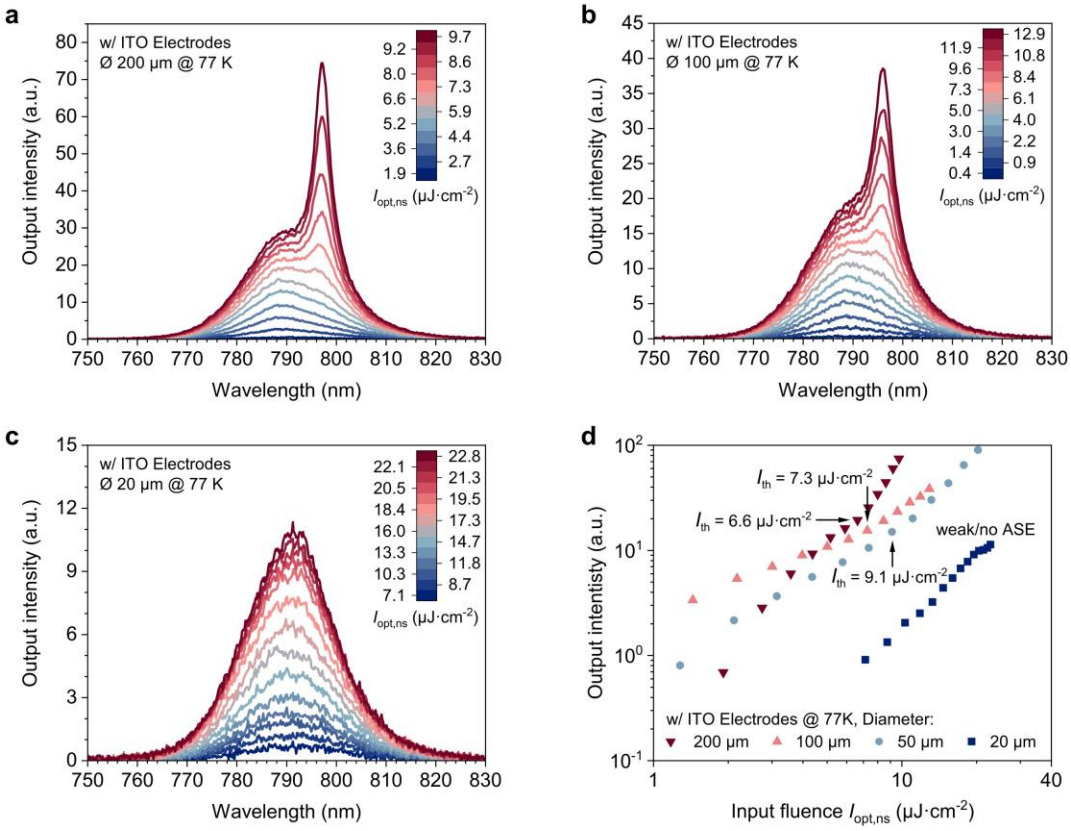

Extended Data Fig. 2 | Optical characterization of PeLED stacks with $I_{opt,ns}$ pump source. a-c, PL output from the contacted PeLED stacks with different active areas at 77 K. **d**, Corresponding light output intensity as a function of input laser fluence ($I_{opt,ns}$).

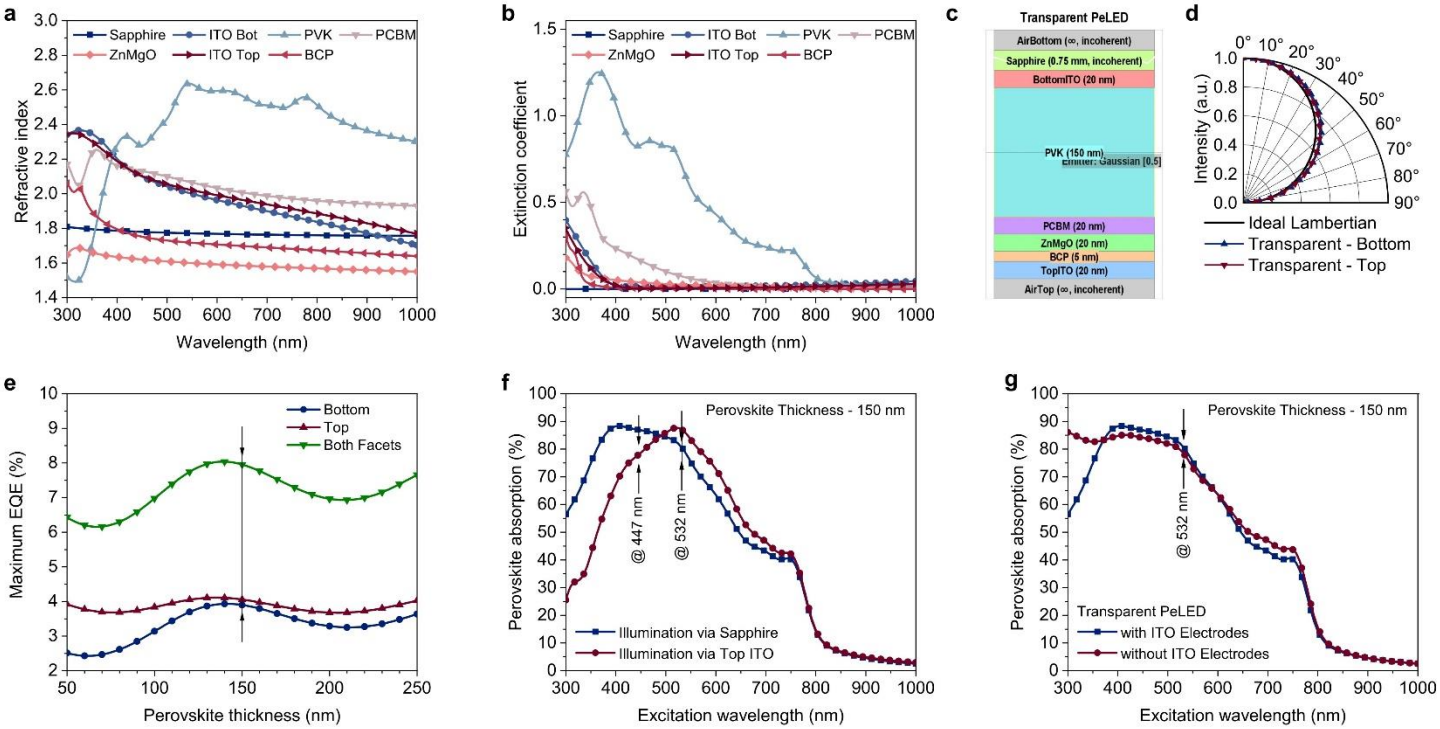

Extended Data Fig. 3 | PeLED optical constants and absorption/emission modeling. a, Refractive indices and **b**, extinction coefficients of other PeLED functional layers. **c**, Layer stack with a broad isotropic dipole distribution in the perovskite layer (PVK) used for the multi-physics modeling. The perovskite reabsorption was set to 0, thereby excluding photon recycling effects. Me-4PACz /Al_xO_y HTL was not factored in due to negligible thickness. **d**, Simulated EL intensity as a function of viewing angle. **e**, Maximum simulated EQE from each device facet for IQE of 100%. **f**, Simulated absorption of the perovskite gain layer of the contacted PeLED as a function of excitation wavelength for the case of sapphire/top ITO light incidence. **g**, Simulated absorption of the perovskite gain layer as a function of excitation wavelength for the contacted and electrode-free PeLED stacks with light impinging from the sapphire side.

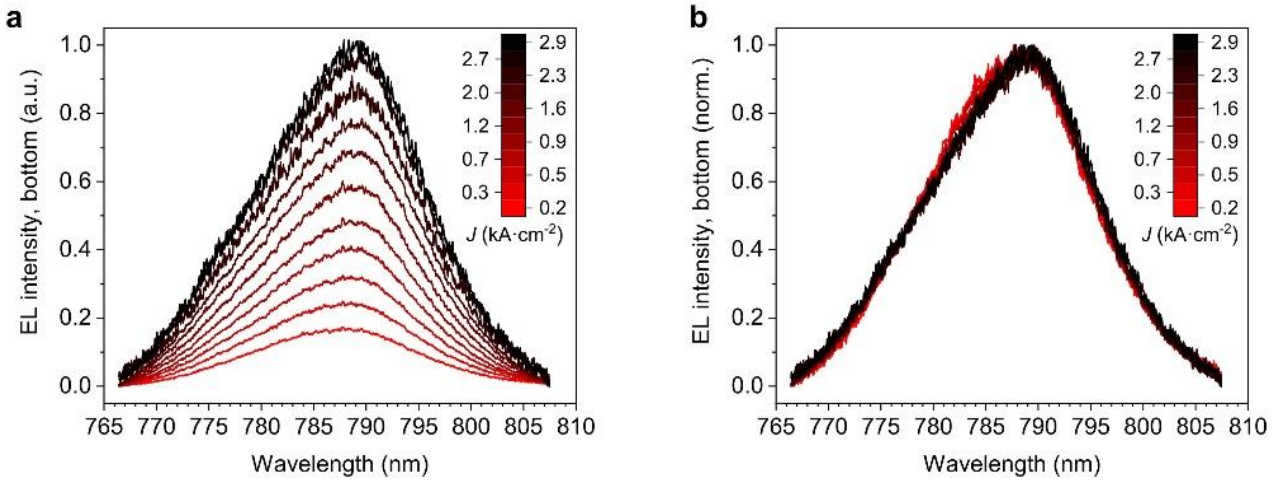

Extended Data Fig. 4 | EL spectra from a ø 50 µm device recorded through the substrate at 77 K. **a**, As-recorded. **b**, Normalized.

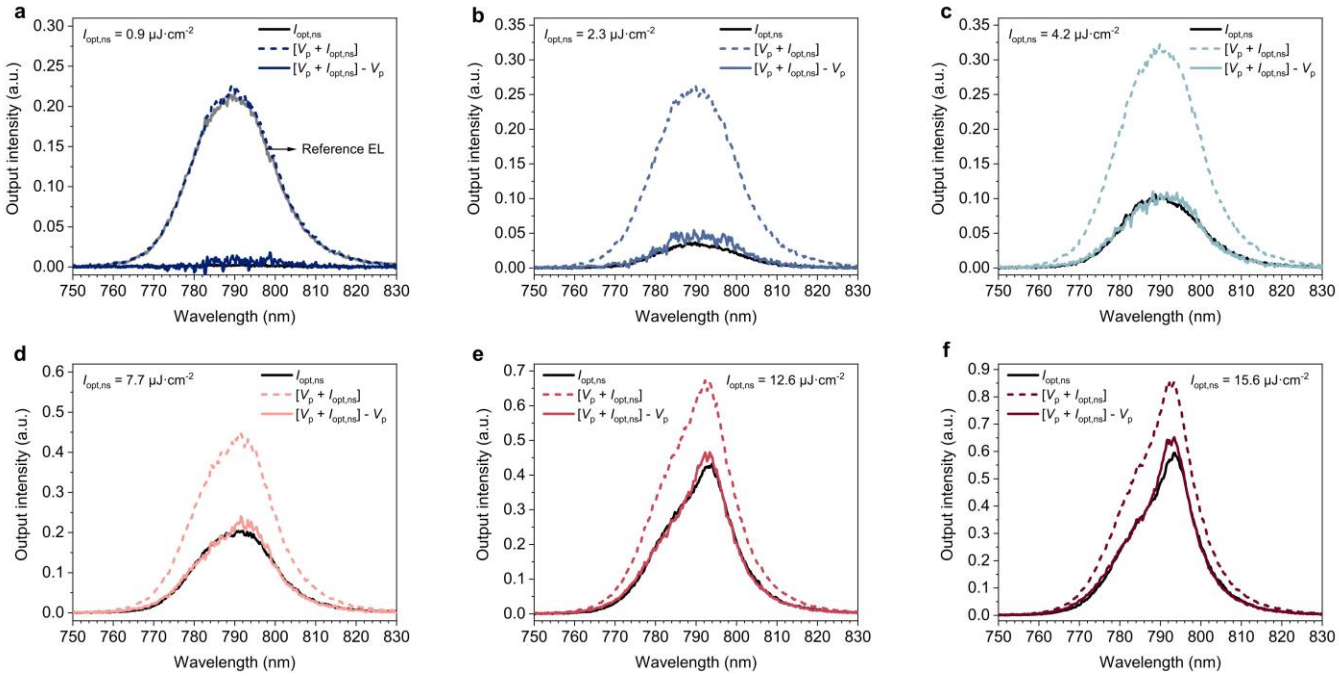

Extended Data Fig. 5 | Photo-electrical co-excitation of contacted PeLED stacks at 77 K. a-f, Standalone optical excitation with variable $I_{opt,ns}$ (black solid lines), photo-electrical spectra at variable $I_{opt,ns}$ and fixed V_p (dashed), and joint spectra adjusted by subtracting the reference EL signal (colored solid lines). The V_p (J = 3.5 kA cm^{-2}) was fixed across these measurements, producing the reference EL signal shown in (**a**) in the absence of optical excitation.

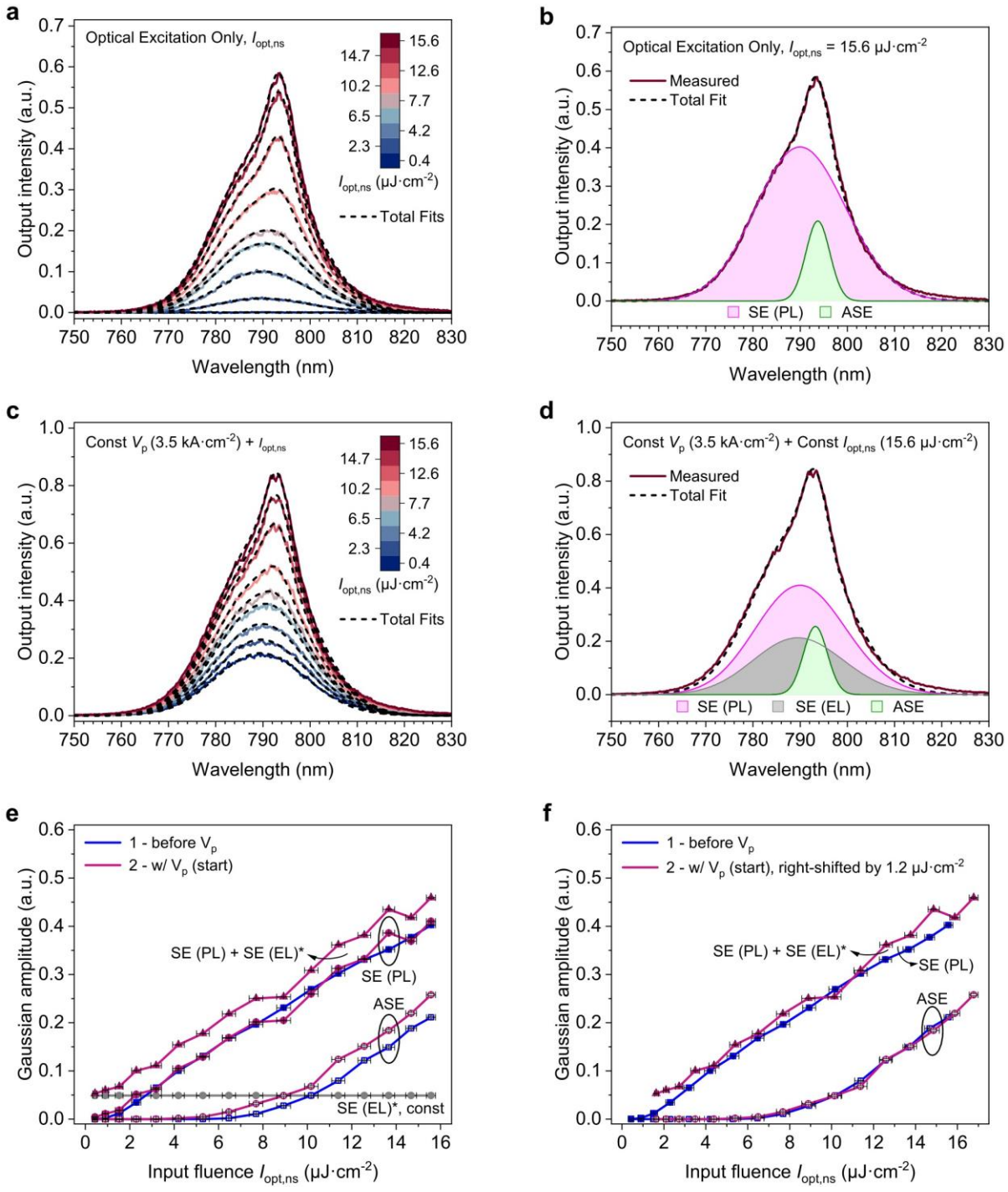

Extended Data Fig. 6 | Deconvolution of PL_{ns} signals under standalone 2.3 ns optical bias and photo-electric co-excitation at the onset of the electrical pulse into two (without V_p) or three (with

***V_p*) Gaussian contributions. a-b,** Exemplary fits at variable $I_{opt,ns}$ without electrical bias. **c-d,** Exemplary fits at variable $I_{opt,ns}$ with electrical bias. **e**, As-extracted, and **f**, right-shifted by 1.2 μJ cm^{-2} Gaussian amplitudes with and without V_p. For SE (PL) and ASE fits, both central energy (wavelength) and standard deviation are fixed. All the parameters of SE (EL) fit are fixed. SE (EL) signal was multiplied by a factor of 0.23 to account for EL contribution to the total signal and is displayed as SE (EL)*. The PL laser pulse duration is 2.3 ns (Supplementary Fig. S7a), whereas the EL+PL signal integration time was 10 ns. The horizontal error bars represent experimental input energy uncertainty, whereas vertical error bars represent one standard deviation for the fitted parameter.

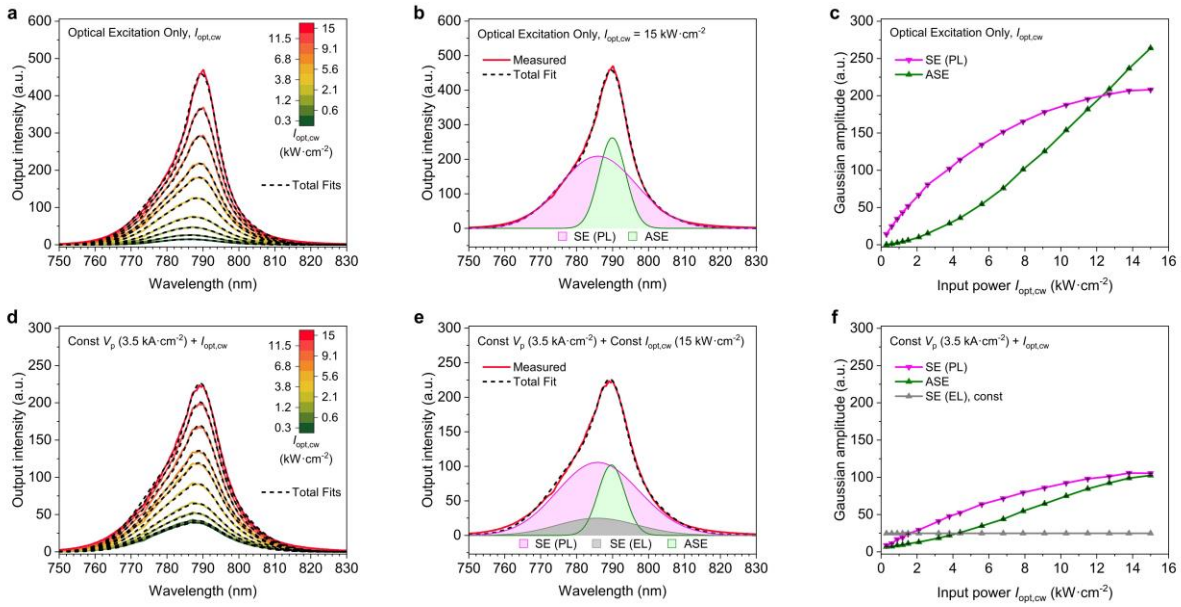

Extended Data Fig. 7 | Deconvolution of PL$_{cw}$ signals under standalone 1 µs CW optical bias and under photo-electric co-excitation into two (without V_p) or three (with V_p) Gaussian contributions. **a-b,** Exemplary fits at variable $I_{opt,cw}$ without V_p. **c,** SE (PL) and ASE Gaussian amplitudes as a function of input laser power $I_{opt,cw}$ without V_p. **d-e,** Exemplary fits at variable $I_{opt,cw}$ with V_p. **f**, SE (PL), SE (EL), and ASE Gaussian amplitudes as a function of input laser power $I_{opt,cw}$ with V_p. For SE (PL) fit, only central energy (wavelength) is fixed; standard deviation and amplitude vary. For ASE fit, both central energy (wavelength) and standard deviation are fixed. All the parameters of SE (EL) fit are fixed. The vertical error bars represent one standard deviation for the fitted parameter.

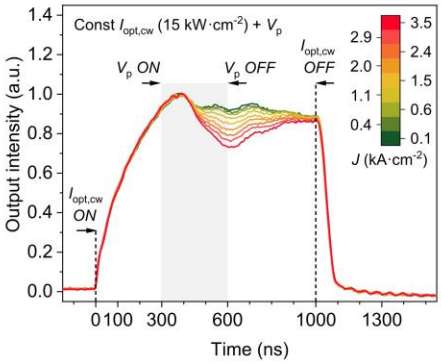

Extended Data Fig. 8 | Transient luminescence response at a constant CW $I_{opt,cw}$ pulse (15 kW cm^{-2}) and variable V_p from 140 to 3500 A cm^{-2}. 300 ns-long electrical pulses are applied 300 ns after the onset of the CW optical pulse.

REFERENCES

1. Min, H. *et al.* Perovskite solar cells with atomically coherent interlayers on SnO2 electrodes. *Nature* **598**, 444–450 (2021).
2. Zhang, T. *et al.* Ion-modulated radical doping of spiro-OMeTAD for more efficient and stable perovskite solar cells. *Science*, 495–501 (2022).
3. Sidhik, S. *et al.* Deterministic fabrication of 3D/2D perovskite bilayer stacks for durable and efficient solar cells. *Science*, 1425–1430 (2022).
4. Cao, Y. *et al.* Perovskite light-emitting diodes based on spontaneously formed submicrometre-scale structures. *Nature* **562**, 249–253 (2018).
5. Wang, K. *et al.* Suppressing phase disproportionation in quasi-2D perovskite light-emitting diodes. *Nat Commun* **14**, 397 (2023).
6. Guo, B. *et al.* Ultrastable near-infrared perovskite light-emitting diodes. *Nat Photonics* **16**, 637–643 (2022).
7. Kim, J. S. *et al.* Ultra-bright, efficient and stable perovskite light-emitting diodes. *Nature* **611**, 688–694 (2022).
8. Liu, Z. *et al.* Perovskite Light-Emitting Diodes with EQE Exceeding 28% through a Synergetic Dual-Additive Strategy for Defect Passivation and Nanostructure Regulation. *Advanced Materials* **33**, 2103268 (2021).
9. Bao, C. *et al.* Bidirectional optical signal transmission between two identical devices using perovskite diodes. *Nat Electron* **3**, 156–164 (2020).
10. Ollearo, R. *et al.* Ultralow dark current in near-infrared perovskite photodiodes by reducing charge injection and interfacial charge generation. *Nat Commun* **12**, 7277 (2021).
11. Lei, L., Dong, Q., Gundogdu, K. & So, F. Metal Halide Perovskites for Laser Applications. *Adv Funct Mater* **31**, 2010144 (2021).
12. Tatarinov, D. A. *et al.* High-Quality CsPbBr3 Perovskite Films with Modal Gain above 10 000 cm−1 at Room Temperature. *Adv Opt Mater* **11**, 2202407 (2023).
13. Liu, Y. *et al.* Ligand assisted growth of perovskite single crystals with low defect density. *Nat Commun* **12**, 1686 (2021).
14. Gao, Y. *et al.* High-Performance Perovskite Light-Emitting Diodes Enabled by Passivating Defect and Constructing Dual Energy-Transfer Pathway through Functional Perovskite Nanocrystals. *Advanced Materials* **34**, 2207445 (2022).
15. Braly, I. L. *et al.* Hybrid perovskite films approaching the radiative limit with over 90% photoluminescence quantum efficiency. *Nat Photonics* **12**, 355–361 (2018).
16. Pourdavoud, N. *et al.* Room-Temperature Stimulated Emission and Lasing in Recrystallized Cesium Lead Bromide Perovskite Thin Films. *Advanced Materials* **31**, 1903717 (2019).
17. Huang, C. Y. *et al.* CsPbBr3 Perovskite Quantum Dot Vertical Cavity Lasers with Low Threshold and High Stability. *ACS Photonics* **4**, 2281–2289 (2017).
18. Kim, H. *et al.* Optically Pumped Lasing from Hybrid Perovskite Light- Emitting Diodes. *Adv Opt Mater* **8**, 1901297 (2019).
19. Cho, C. *et al.* Electrical Pumping of Perovskite Diodes: Toward Stimulated Emission. *Advanced Science* **8**, 2101663 (2021).
20. Jia, Y., Kerner, R. A., Grede, A. J., Rand, B. P. & Giebink, N. C. Continuous-wave lasing in an organic-inorganic lead halide perovskite semiconductor. *Nat Photonics* **11**, 784–788 (2017).
21. Qin, C. *et al.* Stable room-temperature continuous-wave lasing in quasi-2D perovskite films. *Nature* **585**, 53–57 (2020).
22. Allegro, I. *et al.* Distributed Feedback Lasers by Thermal Nanoimprint of Perovskites Using Gelatin Gratings. *ACS Appl Mater Interfaces* **15**, 8436–8445 (2023).

23. Cegielski, P. J. *et al.* Monolithically Integrated Perovskite Semiconductor Lasers on Silicon Photonic Chips by Scalable Top-Down Fabrication. *Nano Lett* **18**, 6915–6923 (2018).
24. Roh, K. *et al.* Widely Tunable, Room Temperature, Single-Mode Lasing Operation from Mixed-Halide Perovskite Thin Films. *ACS Photonics* **6**, 3331–3337 (2019).
25. Goldberg, I. *et al.* Multimode Lasing in All-Solution-Processed UV-Nanoimprinted Distributed Feedback $MAPbI_3$ Perovskite Waveguides. *ACS Photonics* **10**, 1591–1600 (2023).
26. Kim, H. *et al.* Hybrid perovskite light emitting diodes under intense electrical excitation. *Nat Commun* **9**, 4893 (2018).
27. Zhao, L. *et al.* Thermal Management Enables Bright and Stable Perovskite Light-Emitting Diodes. *Advanced Materials* **32**, 2000752 (2020).
28. Zhao, L. *et al.* Nanosecond-Pulsed Perovskite Light-Emitting Diodes at High Current Density. **33**, 2104867 (2021).
29. Elkhouly, K. *et al.* Intense Electrical Pulsing of Perovskite Light Emitting Diodes under Cryogenic Conditions. *Adv Opt Mater* **10**, 2200024 (2022).
30. Zou, C., Liu, Y., Ginger, D. S. & Lin, L. Y. Suppressing Efficiency Roll-Off at High Current Densities for Ultra-Bright Green Perovskite Light-Emitting Diodes. *ACS Nano* **14**, 6076–6086 (2020).
31. Zhao, L. *et al.* Thermal Properties of Polymer Hole-Transport Layers Influence the Efficiency Roll-off and Stability of Perovskite Light-Emitting Diodes. *Nano Lett* **23**, 4785–4792 (2023).
32. Ahn, N. *et al.* Optically Excited Lasing in a Cavity-Based, High-Current-Density Quantum Dot Electroluminescent Device. *Advanced Materials* **35**, 2206613 (2023).
33. Slowik, I. *et al.* Novel organic light-emitting diode design for future lasing applications. *Org Electron* **48**, 132–137 (2017).
34. Lee, J. H., Ke, T. H., Genoe, J., Heremans, P. & Rolin, C. Overlapping-Gate Organic Light-Emitting Transistors. *Adv Electron Mater* **5**, 1800437 (2019).
35. Schols, S. *et al.* An organic light-emitting diode with field-effect electron transport. *Adv Funct Mater* **18**, 136–144 (2008).
36. Goldberg, I. *et al.* Active area dependence of optoelectronic characteristics of perovskite LEDs. *J Mater Chem C Mater* **9**, 12661–12670 (2021).
37. Elkhouly, K. *et al.* Operationally Stable Perovskite Light Emitting Diodes with High Radiance. *Adv Opt Mater* **9**, 2100586 (2021).
38. He, Y. *et al.* Perovskite Light-Emitting Diodes with Near Unit Internal Quantum Efficiency at Low Temperatures. *Advanced Materials* **33**, 2006302 (2021).
39. Jia, Y., Kerner, R. A., Grede, A. J., Rand, B. P. & Giebink, N. C. Factors that Limit Continuous-Wave Lasing in Hybrid Perovskite Semiconductors. *Adv Opt Mater* **8**, 1901514 (2020).
40. Brenner, P. *et al.* Continuous wave amplified spontaneous emission in phase-stable lead halide perovskites. *Nat Commun* **10**, 988 (2019).
41. Ahn, N. *et al.* Electrically driven amplified spontaneous emission from colloidal quantum dots. *Nature* **617**, 79–85 (2023).
42. Peters, G. I. & Allen, L. Amplified spontaneous emission I. the threshold condition. *Journal of Physics A: General Physics* **4**, 238–243 (1971).
43. Frolov, S. V, Vardeny, Z. V & Yoshino, K. *Cooperative and stimulated emission in poly"p-phenylene-vinylene… thin films and solutions*. (1998).
44. Bourdakos, K. N., Cury, L. A. & Monkman, A. P. The dependence of the amplified spontaneous emission on the waveguide excitation length for high quantum efficiency conjugated polymers. *Org Electron* **12**, 1142–1145 (2011).
45. Xie, M. *et al.* High-Efficiency Pure-Red Perovskite Quantum-Dot Light-Emitting Diodes. *Nano Lett* **22**, 8266–8273 (2022).

46. Whitworth, G. L., Dalmases, M., Taghipour, N. & Konstantatos, G. Solution-processed PbS quantum dot infrared laser with room-temperature tunable emission in the optical telecommunications window. *Nat Photonics* **15**, 738–742 (2021).

Experimental Methods

Materials.

Lead iodide (PbI_2) and [4-(3,6-Dimethyl-9H-carbazol-9-yl)butyl] phosphonic acid (Me-4PACz) were purchased from Tokyo Chemical Industry (TCI). Formamidinium chloride (FACl), formamidinium iodide (FAI), methylammonium chloride (MACl), 2-thiopheneethylammonium chloride (TEACl) were purchased from Greatcell Solar Materials. Lead bromide ($PbBr_2$) and lithium fluoride (LiF) were purchased from Sigma Aldrich. Cesium iodide (CsI) was purchased from abcr GmbH. Bathocuproine (BCP) was purchased from Luminescence Technology Corp. (Lumtec). 6,6'-phenyl-C61-butyric acid methyl ester (PCBM) was purchased from Nano-C Inc. Zinc acetate dihydrate, magnesium acetate tetrahydrate, tetramethylammonium hydroxide (TMAH), ethyl acetate, dimethyl sulfoxide (DMSO), chlorobenzene, dimethylformamide (DMF), 1-methyl-2-pyrrolidone (NMP), ethanol (EtOH), and isopropyl alcohol (IPA) were purchased from Sigma Aldrich. All materials were used as received.

Perovskite Solution Preparation.

$Cs_{0.1}FA_{0.9}PbI_{2.855}Br_{0.145}$ perovskite was prepared by dissolving 418 mg FAI, 70.2 mg CsI, 71.8 mg $PbBr_2$, 54.7 mg MACl, and 1145 mg PbI_2 in 2.0 mL mixed solvents (DMF: NMP = 9:1, volume: volume). The perovskite precursor was stirred overnight at room temperature. The precursor was diluted to 0.5 M prior to spin-coating.

PeLED Fabrication.

Bottom contact layout fabrication. Sapphire substrates with high thermal conductivity are used to mitigate the detrimental effects of Joule heating during electrical operation. Bottom metallic contact lines were DC-magnetron sputtered over the substrates and patterned using a lift-off approach. A thin ITO electrode was then RF-magnetron sputtered to obtain a 20 nm-thick PeLED contact with a 350 ± 20

Ω sq^{-1} sheet resistance. ITO was etched in a CH_4-based ICP-RIE plasma. 100 nm-thick pixel definition layer - Al_2O_3 - was grown via atomic layer deposition at 150 °C using trimethylaluminum and H_2O precursors. Finally, the contact pads and device circular areas were defined using a wet etch process based on TMAH chemistry.

Deposition of PeLED functional layers. The pixel-defined substrates were cleaned in ultrasonic baths of detergent, deionized water, acetone, and IPA successively for 10 minutes in each bath; blow-dried with N_2; and exposed to O_2 plasma (200 W). Then, the substrates were transferred to an inert glovebox environment. Me-4PACz solution (1 mmol L^{-1} in anhydrous EtOH) was sonicated at 30 °C for 10 min before usage. Then, it was spin-coated on sapphire/ITO pixel-defined substrates at a speed of 3000 rpm for 30 s, followed by annealing at 100 °C for 10 min. Al_xO_y nanoparticles, diluted to 1:40 (volume:volume) by the addition of IPA, were spin-coated at 3000 rpm to improve Me-4PACz wettability, followed by annealing at 100 °C for 10 minutes. We introduce 2-thiopheneethylammonium chloride (TEACl) and formamidinium chloride (FACl) interfacial modification layers to improve the perovskite surface properties and suppress nonradiative recombination[47]. 1.0 mg mL^{-1} of TEACl in anhydrous IPA was spin-coated at a speed of 3000 rpm for 30 s, followed by annealing at 100 °C for 10 min. The perovskite films were prepared by gas quenching method according to our previous work[47]. Briefly, the perovskite precursor was dynamically spun onto the substrates, followed by an N_2 quenching process for 30 s. Then, the perovskite films were annealed at 120 °C for 70 min. The perovskite top surface was treated first by FACl (0.5 mg mL^{-1} in anhydrous IPA). FACl was dynamically spin-coated onto the substrates at a speed of 3000 rpm for 30 s, followed by annealing at 120 °C for 25 min. In addition to the FACl treatment, the perovskite surface was further modified by TEACl, where 1.0 mg mL^{-1} of TEACl in anhydrous IPA was spin-coated at a speed of 3000 rpm for 30 s, followed by annealing at 110 °C for 3 min. Then, 15 mg ml^{-1} PCBM solution in chlorobenzene and the ZnMgO nanoparticle solution, prepared according to our previously reported protocol[37], were

consecutively spin-coated onto the perovskite layer at 3000 rpm and 4000 rpm, respectively. Electron injection from the top ITO electrode is facilitated by the incorporation of a 5 nm-thick insulating bathocuproine (BCP) buffer layer, which also reduces the top ITO bombardment impact on the underlying layers. BCP buffer layer was thermally evaporated at a rate of 0.5 Å s^{-1}. Afterward, a 20 nm-thick ITO cathode was DC-magnetron sputtered via a shadow mask, obtaining $R_{sheet} \approx 600\ \Omega\ sq^{-1}$. PeLED was concluded by thermal evaporation of 100 nm-thick Al via another shadow mask. The complete PeLED fabrication details, including a step-by-step schematic, can be found in Supplementary Fig. S2.

Optical Characterization.

The sample was mounted into a JANIS VPF-100 cryostat. The cryostat was pumped down to a pressure of 10^{-4} mbar and liquid N_2 was used to cool down the sample to 77 K. A Lakeshore 335 temperature controller and a silicon diode temperature sensor anchored above the sample position were used to set and control the sample temperature. ASE characterizations were done using a Q-switched laser (CryLaS FTSS 355-300; 2.3 ns in FWHM; 20 Hz), which produces frequency-doubled pulses at a 532 nm wavelength. The laser beam was focused into a Gaussian spot with an FWHM diameter of 400 μm. The PL emerging from the sample was imaged by a microscope equipped with a Mitutoyo 10X infinity corrected objective (f = 20 mm) coupled with a tube lens (f = 200 mm). The imaged PL was focused on the entrance slit of an imaging spectrometer (Teledyne Princeton Instruments SpectraPro HRS-500), and the spectra were recorded using a digital intensified camera (Teledyne Princeton Instruments PI-MAX 4 with a spectral resolution of 0.03 nm). For scattering loss measurements, the sample was excited using a 300×50 μm^2 stripe. For CW optical measurements, a high-power laser diode (L450G1 from Thorlabs; 447 nm) was focused into a 120×30 μm^2 stripe. A Keithley 2520 laser diode driver was used to send high-power optical pulses at a frequency of 20 Hz. PL was collected in a similar fashion to nanosecond optical excitation measurements.

Pulsed Electrical Characterization.

The sample was mounted in the same setup that was used for optical characterization. In addition, an AV-1011-B1-B voltage pulser from AVTECH was used to electrically pump the PeLEDs through 50 Ω coaxial cables. The photodiode signal (SM05PD1B from Thorlabs) was then amplified using DHPCA-100 variable gain transimpedance amplifier from FEMTO. The voltage, current, and photodiode signals were synchronously collected using a Keysight DSOX3014T oscilloscope. The current was measured using a 50 Ω termination into the oscilloscope. All pulsed measurements were done at a frequency of 10 Hz, and each data point was recorded after 50 pulses to ensure measurement reproducibility. The EQE was calculated using the stabilized part of the photodiode and current pulses before the pulse termination. For short electrical pulses (≤ 500 ns), current transients do not fully saturate. Therefore, we extrapolate the current values from the series resistance I-V regime at high voltages. For EQE calculation, the photodiode signal was carefully calibrated by fixing the detector position. The spectrum at each temperature was used for EQE calculation according to our previously reported method[29]. A global calibration factor was taken into account by comparing the EQE measured by an integrating sphere inside the glovebox to the one measured at room temperature inside the cryostat.

Photo-Electrical Co-excitation.

For the nanosecond co-excitation, the laser source (CryLaS FTSS 355-300, 2.3 ns in FWHM, 20 Hz) was used to trigger the voltage pulser (AV-1011-B1-B from AVTECH). The laser source was coupled to a 200 m-long optical fiber (FG200UCC, 0.22 NA from Thorlabs) to induce a 1 μs delay for the optical pulse. This delay allowed controlling the co-excitation timing by tuning the delay of the electrical pulse within 1 μs, which is longer than the typical pulse widths used at high current density operation. The signal collection was done similarly to optical/electrical characterization experiments, except for the gating window of the spectrometer that was limited to 10 ns and was triggered 2 ns before the onset of the optical pulse. For the CW co-excitation, the laser diode source (L450G1 from Thorlabs; 447 nm)

was used to trigger the voltage pulser (AV-1011-B1-B from AVTECH). The spectrometer's gating window was configured to correspond to the electrical pulse width (300 ns).

Structural Measurements.

Top-view SEM characterization of the perovskite gain layer was performed using FEI Nova 200 scanning electron microscope system. The material was spin-coated over a Si/SiO_2 substrate. RC2 ellipsometer from J.A. Woollam was used to extract n, k coefficients, and thicknesses of PeLED functional layers.

Simulation and Curve Fittings.

Light outcoupling simulations. To simulate PeLED outcoupling ($f_{\text{outcoupled}}$) and EL angular distribution, optical modeling was performed in the commercial software Setfos from Fluxim. Homogeneous dipole distribution was assumed in the perovskite emission layer and the reabsorption was set to 0, thereby excluding photon recycling, which was shown to increase the outcoupling by a factor of ~ 1.3 (lowering the IQE estimations accordingly) in PeLEDs with 150 nm-thick emissive layers[48]. The thicknesses and n, k parameters, extracted by spectroscopic ellipsometry, were integrated into the model (Extended Fig. 4). The absorption module was used to calculate the photon flux across the device. The IQE of a PeLED can be estimated by adjusting the EQE for $f_{\text{outcoupled}}$[26]:

$$IQE = \frac{EQE}{f_{\text{outcoupled}}}.$$

Mode simulations. In order to determine the fundamental TE_0 mode characteristics of perovskite device configurations, we employed a Finite Difference Eigenmode (FDE) solver in Ansys Lumerical. The refractive indices and extinction coefficients of each layer, as depicted in Extended Fig. 4a-b, were incorporated into the model. However, the perovskite layer's absorption was disregarded and set to zero,

mimicking a transparency condition, which allowed for the loss assessment solely from the surrounding layers. The mode confinement factor (Γ) was calculated using the following equation:

$$\Gamma = \frac{\int_{PVK}|E|^2 \cdot dt}{\int|E|^2 \cdot dt},$$

where $|E|^2$ is the electric field intensity of the fundamental TE_0 mode. The optical propagation losses α (in cm^{-1}) were calculated from the following equation:

$$\alpha = -\frac{4\pi}{\lambda} Im(n_{\text{eff}}).$$

Gaussian fitting. Emitted spectra from 2.3 ns (PL_{ns}) and CW (PL_{cw}) optical (co)-excitation experiments were fitted as a sum of two (without electrical bias) or three (with additional SE (EL) electrical bias contribution) Gaussian functions with amplitudes A_1, A_2, and A_3, standard deviations σ_1, σ_2, and σ_3, and peak positions E_1, E_2, and E_3:

$$\text{PL}_{\text{ns/cw}}(E) = \text{SE (PL)} + \text{ASE} + \text{SE (EL)},$$

$$\text{PL}_{\text{ns/cw}}(E) = A_1 \cdot exp\left(-\frac{(E-E_1)^2}{2{\sigma_1}^2}\right) + A_2 \cdot exp\left(-\frac{(E-E_2)^2}{2{\sigma_2}^2}\right) + A_3 \cdot exp\left(-\frac{(E-E_3)^2}{2{\sigma_3}^2}\right),$$

where each of A_i, E_i, and σ_i describe the amplitude, peak position, and standard deviation of the corresponding Gaussian functions. The fit accuracy is improved by restricting the number of fitting parameters to 2 or to 3 for ns and CW optical (co)-excitation experiments, respectively. For the 2.3 ns excitation, the only fitting parameters were A_1 and A_2 or SE (PL) and ASE amplitudes. When using CW excitations, an extra σ_1 parameter or the standard deviation of SE (PL) contribution is fitted due to notable SE (PL) linewidth broadening at higher CW optical powers relative to 2.3 ns excitation. A fixed SE (EL) Gaussian contribution is inferred from the lowest optical excitation point where the SE (PL) and ASE contributions are negligible. Finally, the fitting takes place within the energy space and is then converted back into a wavelength domain by using a Jacobian transformation:

$$\lambda = \frac{hc}{E} \Rightarrow d\lambda = -\frac{hc}{E^2} dE.$$

The horizontal error bars are calculated by estimating the experimental error in tuning input fluence, whereas vertical error bars represent one standard deviation for the fitted parameter, calculated by taking the square root of the parameter's diagonal element in the covariance matrix.

Data Availability

Source data for main and extended figures are provided with the paper. All other data supporting the findings of this study are available from the corresponding authors upon reasonable request.

Methods-only References

47. Zhang, X. *et al.* Minimizing the Interface-Driven Losses in Inverted Perovskite Solar Cells and Modules. *ACS Energy Lett* **8**, 2532–2542 (2023).
48. Cho, C. *et al.* The role of photon recycling in perovskite light-emitting diodes. *Nat Commun* **11**, 611 (2020).